Morphing Wings: A Study Using Aerodynamic Shape Optimization

Nathanael J. Curiale* and David W. Zingg†
Institute for Aerospace Studies, University of Toronto
4925 Dufferin St., Toronto, Ontario, M3H 5T6, Canada

With the aviation industry under pressure to reduce environmental impact, morphing wings have the potential to improve aircraft performance, thereby making a contribution to reducing carbon dioxide emissions. Through high-fidelity aerodynamic shape optimization, various forms of morphing wings are assessed for a hypothetical regional-class aircraft. The framework used solves the Reynolds-averaged Navier-Stokes equations and utilizes a gradient-based optimization algorithm. Baseline geometries are developed through a multipoint optimization where the average drag coefficient is minimized over a range of 27 flight conditions with additional dive constraints. Morphing optimizations are then performed, beginning with these baseline shapes. Five distinct types of morphing are investigated and compared. Overall, a theoretical fully adaptable wing produces roughly a 2% improvement in average cruise performance, whereas trailing-edge morphing results in just over a 1% improvement in average cruise performance. Trailing-edge morphing proves to be more beneficial than leading-edge morphing, upper-surface morphing, and a sealed flap.

I. Introduction

The aviation industry is faced with great pressure to reduce global fuel consumption. In 2011 alone, the aviation industry produced 676 million tonnes of global CO_2 emissions.[1] Although there has been significant effort to minimize the effect on the planet, drastic improvements are still required. Reducing fuel consumption can introduce benefits on two main fronts. From an environmental standpoint, the amount of fuel an aircraft consumes is directly related to the amount of carbon-dioxide emissions emitted. From an economic standpoint, reducing fuel burn will have a large influence on the aviation industry, as fuel is one of the largest portions of their operating cost. One technology that has shown promise in reducing aircraft fuel consumption is morphing wings. This paper will focus on morphing wings in order to quantify the effectiveness of this technology and provide insights to further research.

The concept of morphing wings has been around for quite a long time. The Wright brothers experimented with morphing wings in their initial aircraft by using twist to control the roll of their aircraft. Since then, multiple modes of morphing have been experimented with. Morphing methods such as sweep, span, chord, pitch, gull, camber and combinations of these parameters have been implemented and tested.[2] These types of systems have been experimented with on all types of aircraft, from fighter jets to small UAVs. They each allow for a smooth transition between the wing surface and the morphing surface, differing from traditional devices such as flaps and slats. In recent years, some morphing wing actuators have become very robust, such as FlexFoil made by FlexSys Inc. It is currently undergoing testing and is predicted to enable about a 3% reduction in fuel burn on a retrofitted business jet wing.[3] Wing morphing actuators that adapt the sectional shape of a wing have physically been tested and are seen as more viable options than other extreme forms of wing morphing, such as span and sweep adaptations.

Several computational studies have been completed, such as the work of Lyu and Martins.[4] They looked at the possibility of using an adaptive morphing trailing-edge on a Boeing 777-LR. The results varied de-

*MASc Graduate, nathan.curiale@utoronto.ca
†University of Toronto Distinguished Professor of Computational Aerodynamics and Sustainable Aviation, Director, Centre for Research in Sustainable Aviation, dwz@oddjob.utias.utoronto.ca

pending on the conditions. A drag reduction of 1% resulted at on-design conditions and a drag reduction of 5% resulted at off-design conditions. Apart from this, the variable camber continuous trailing edge flap (VCCTEF) system developed by a group at NASA Ames Research Center was studied by Rodriguez et al.[5] They completed a study which compared the most optimal wing performance at off-design conditions to the performance of a wing, initially designed for mid-cruise conditions, that uses the VCCTEF actuation system to improve performance. In total, based solely on aerodynamics, there was roughly a 3-6% drag reduction between the mid-cruise designed wing evaluated at off-design conditions and the wing shape when morphing was involved at off-design conditions as well as under a drag count difference between the morphed wing and the most optimal wing at off-design conditions.

Studies have also included morphing of other parts of the wing such as the leading edge or the upper surface. Kintscher[6] shows that leading-edge morphing, also known as leading-edge droop, can increase the C_{Lmax} by 25%. As well, Stanewsky talks about a study completed by Airbus on a A340 wing[7] where the group investigated an upper surface "shock bump" and achieved a 4% drag reduction at off-design cruise conditions. Zingg et al.[8] also completed a two-dimensional study on full upper surface morphing where the morphed designs were compared against a multipoint optimized design. This lead to a profile drag reduction of 4-5% across the entire Mach number range. Another interesting idea is the Adaptive Dropped Hinge Flap (ADHF) that was developed by Airbus for their A350.[9] This actuator uses a normal flap but also introduces a spoiler to cover the gap between the wing and the flap as much as possible, which has a significant impact on drag reduction. This concept is a very simple approach of obtaining a morphing wing compared to the more complex actuation systems mentioned earlier. All these types of morphing are viable solutions and this work looks to make quantifiable comparisons between each based on the average performance changes seen throughout the entire flight envelope.

A common theme in these past studies is that the benefits of morphing are higher at off-design conditions. Because of this, it makes sense that aircraft which vary largely from their nominal design cruise flight condition should benefit more from morphing technology. By looking at the typical operating conditions of general aircraft, it is evident that regional jets experience a wider range of flying conditions relative to other types of aircraft. Regional jet flight plans are shorter than long-haul aircraft meaning they spend a larger percentage of their time in variable flight conditions relative to cruise. This makes regional jets a suitable candidate for morphing technology. In addition, the previous studies typically emphasized large long-haul aircraft. For these reasons, the aim of this work is to assess the use of morphing wings on regional jet aircraft and explore the avenues in which the potential benefits of morphing can be achieved.

II. Optimization Methodology

The aerodynamic shape optimization framework called Jetstream, which was developed at the University of Toronto Institute of Aerospace Studies, is used for this work. Major contributions to this framework include Hicken and Zingg,[10,11] M. Osusky and Zingg,[12] L. Osusky et al.[13] and Gagnon and Zingg.[14] This framework has been used for many different aerodynamic shape optimization cases, such as the AIAA Aerodynamic Design Optimization Discussion Group,[15] drag minimization of non-planar wings,[14,16] and the optimization of unconventional aircraft.[14,17] The framework provides robust geometrical surface representations, efficient flow solutions, and an efficient optimization scheme and is thus suitable to address the complex nature of morphing wings in high Reynolds number flows.

Jetstream comprises three main components: a geometry parameterization and mesh movement scheme, a flow solver for the Reynolds-Averaged Navier-Stokes (RANS) equations, and a gradient evaluation and gradient-based optimization scheme. These components are completed sequentially for each iteration of the optimization process.

Basis-spline (B-spline) surfaces are used to parameterize the aerodynamic surfaces. In turn, these B-spline surface points are used as the design variables throughout the optimization. As these design variables change throughout an optimization, the corresponding grid must also be changed accordingly. In order to do this, the grid is embedded in B-spline volumes which are modelled as linear elastic solids, as implemented by Truong et al.[18] and Hicken and Zingg.[11]

The Reynolds-averaged Navier-Stokes equations are solved using the flow solver called Diablo.[10,19] This flow solver uses a two-phase Newton-Krylov method with pseudo-transient continuation to achieve a steady-state solution. GMRES is used to obtain the solution update at every non-linear iteration. The Spalart-Allmaras one-equation turbulence model is used to model turbulent eddy viscosity. Fully turbulent flow is assumed.

The optimization algorithm used is the framework called SNOPT.[20] This framework is a third-party software developed to solve large-scale nonlinear optimization problems through the use of sequential quadratic programming (SQP). In order to use SNOPT, the discrete-adjoint method is first used to calculate all required gradients at a cost which is independent of the number of design variables. These components allow the computation of the gradients for any functional, including the objective and any flow-dependent constraints, which are then passed to SNOPT.

III. Problem Definition

A. Overview

This section gives an overview of the optimization problem formulation. First, a baseline wing shape is optimized and evaluated at a range of flight conditions. Subsequently, this baseline wing shape becomes the initial shape for further optimizations where only portions of the wing are allowed to move in constrained ways consistent with morphing. These subsequent optimizations are performed at multiple flight conditions consistent with the range of conditions the baseline wing was evaluated at. The difference in performance between the baseline and morphed wings then demonstrates the overall aerodynamic benefit morphing can produce.

B. Flight Envelope and Geometry

This work looks at a general aerodynamic optimization problem of a hypothetical regional class aircraft where the coefficient of drag is minimized with C_L and C_M constraints. The aircraft is closely modeled after the Embraer 190 (E190); data provided on this aircraft is used to generate a set of typical flight conditions. The maximum and minimum values for Mach number, altitude and weight that are seen in the E190 aircraft planning manual[21] and available flight data are used to help define the flight envelope. These are shown in Table 1. When specifying individual flight conditions within this flight envelope, a combination of a single Mach number, a single weight and a single altitude are specified. From here, an air density, airspeed and Reynolds number can be computed with the US Standard Atmosphere 1976 atmospheric model.[22] These parameters are then used to calculate values for C_L for each flight condition.

The E190 wing geometry and mesh were taken from past optimization cases of Reist and Zingg who completed various grid refinement and validation studies.[17] The geometry corresponds to the E190 planform and area but initially uses the SC(2)-0012 airfoil at the root and crank, and the SC(2)-0010 airfoil at the tip. The initial wing geometry is shown in Figure 1. The grid corresponding to this geometry, at the optimization level, involves approximately 1.5×10^6 nodes split into 112 blocks with a maximum of about 16000 nodes per block. This grid is also ensured to have $y^+ \approx 1.0$ and leading and trailing-edge spacings $\approx 0.15\%$ chord. While the optimizations are performed on this grid, all results presented are based on an estimated grid-independent solution computed using Richardson extrapolation.

All optimizations minimize the drag coefficient subject to C_L and C_M constraints and a series of geometric constraints dependent on the case. Results are described in terms of C_D as well as ML/D, which relates to the Breguet range equation when the velocity, V, is converted to a Mach number, M. To better estimate the full aircraft ML/D value, the drag coefficient for the rest of the aircraft is estimated at each flight condition and added to the optimized wing drag coefficients. These estimates are calculated by using the process described by Raymer.[23] The general equation is:

$$C_D = F_F \ C_f \ \frac{S_{\text{wet}}}{S_{\text{ref}}} \tag{1}$$

To estimate the drag coefficient for a specific component, the form factor, F_F, and the friction coefficient, C_f, must be found along with the component's wetted area, S_{wet}, and the reference area, S_{ref}. F_F is defined based on geometric dimensions where the C_f is calculated by the Mach number corrected Prandtl-Schlichting relation.[23] As the C_f and F_F are independent, the corresponding friction and pressure drag coefficient can be found as well by:

$$C_{Df} = C_f \ \frac{S_{\text{wet}}}{S_{\text{ref}}} \tag{2}$$

Table 1: Details of the initial geometry and flight envelope.

Geometry		
Planform Area	1000	ft^2
Total Span	94	ft
MAC	13.1	ft
Aspect Ratio	8.8	-
Sweep Angle	28	deg
Mach Number		
Max. Mach Number	0.82	-
Min. Mach Number	0.74	-
Aircraft Weight		
Max. Weight	110,900	lbs
Min. Weight	61,500	lbs
Altitude		
Max. Altitude	41,000	ft
Min. Altitude	31,000	ft

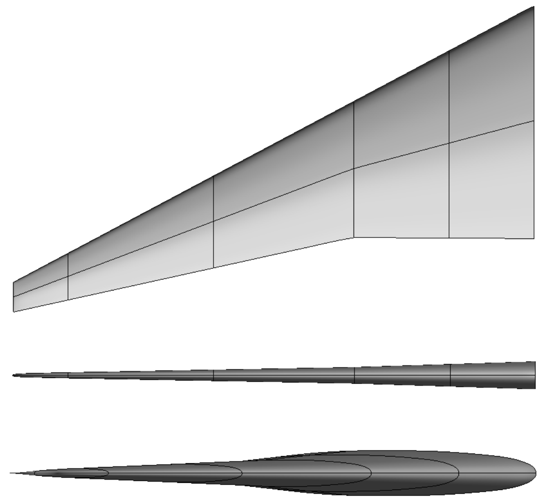

Figure 1: Initial wing planform shape.

$$C_{Dp} = (F_F - 1)\ C_f\ \frac{S_{\text{wet}}}{S_{\text{ref}}} \tag{3}$$

All reported drag values in this work include these estimates for the aircraft.

C. Baseline Wing

The baseline shape is developed through the integral weighting method of Buckley and Zingg,[24] which allows for optimization over a range of operating conditions. In this method, the following integral is minimized:

$$\int_{A1}^{A2}\int_{W1}^{W2}\int_{M1}^{M2} \mathcal{F}\left(M,W,A\right)\mathcal{Z}\left(M,W,A\right)dM\,dW\,dA \tag{4}$$

The function, $\mathcal{F}$, is minimized and depends on a range of cruise altitudes, A, aircraft weights, W, and Mach numbers, M. The function, $\mathcal{Z}$, describes a user-defined weighting in the flight envelope dependent on the priorities of the designer. Defining these ranges of interest is extremely important when focusing on practical aerodynamic designs, as an aircraft will experience variable cruise conditions. The objective function is an approximation to the integral in Eq.(4) as follows:

$$\mathcal{J} = \sum_{i=1}^{N_M}\sum_{j=1}^{N_W}\sum_{k=1}^{N_A} \mathcal{T}_{i,j,k}\left(M_i,W_j,A_k\right)\mathcal{F}\left(M_i,W_j,A_k\right)\mathcal{Z}\left(M_i,W_j,A_k\right)\Delta M\,\Delta W\,\Delta A \tag{5}$$

where N_M, N_W, and N_A are the number of quadrature points used, and ΔM, ΔW, ΔA are the quadrature point spacings in each direction. $\mathcal{T}_{i,j,k}$ is the weight matrix based on the quadrature rule used to approximate the integral. In this work, trapezoidal quadrature is utilized, the user-defined function, $\mathcal{Z}$, is set to unity, and the function, $\mathcal{F}$, is set as the drag coefficient, C_D.

1. Baseline Constraints

For these optimization cases, the airfoil section is changed throughout the optimizations by assigning all parameterized B-spline control points as design variables and allowing only the section shape, in the vertical direction, to change. Constraints placed on the optimization include design variable bound constraints to prevent unrealistic design variable values during early optimization iterations, a volume constraint to meet

Table 2: Design variables and constraint descriptions for the baseline optimization.

	Lower bound	Variable/ Constraint	Upper bound	#
Variables	-5.0°	AoA	+5.0°	29
	-2.0 $z_{\min}$	CPs z	+2.0 $z_{\max}$	714
Constraints	-	C_L	-	29
	-0.175	C_M	-	29
	-	M_{max}	1.4	2
	375 ft^3	Volume	-	1
	+0.8 t_{orig}	Thickness	+1.5 t_{orig}	325
	-	Linear LE/TE	-	2

Table 3: Flight conditions for the 27-point design.

#	ID	M(-)	W(lbs)	A(ft)	C_{L}(-)	#	ID	M(-)	W(lbs)	A(ft)	C_{L}(-)
1	M1_W1_A1	0.74	61500	31000	0.26634	15	M2_W2_A3	0.78	86200	41000	0.53933
2	M1_W1_A2	0.74	61500	36000	0.33654	16	M2_W3_A1	0.78	110900	31000	0.43219
3	M1_W1_A3	0.74	61500	41000	0.42757	17	M2_W3_A2	0.78	110900	36000	0.54610
4	M1_W2_A1	0.74	86200	31000	0.37325	18	M2_W3_A3	0.78	110900	41000	0.69382
5	M1_W2_A2	0.74	86200	36000	0.47164	19	M3_W1_A1	0.82	61500	31000	0.21690
6	M1_W2_A3	0.74	86200	41000	0.59922	20	M3_W1_A2	0.82	61500	36000	0.27408
7	M1_W3_A1	0.74	110900	31000	0.48017	21	M3_W1_A3	0.82	61500	41000	0.34821
8	M1_W3_A2	0.74	110900	36000	0.60673	22	M3_W2_A1	0.82	86200	31000	0.30398
9	M1_W3_A3	0.74	110900	41000	0.77086	23	M3_W2_A2	0.82	86200	36000	0.38410
10	M2_W1_A1	0.78	61500	31000	0.23972	24	M3_W2_A3	0.82	86200	41000	0.48800
11	M2_W1_A2	0.78	61500	36000	0.30291	25	M3_W3_A1	0.82	110900	31000	0.39105
12	M2_W1_A3	0.78	61500	41000	0.38484	26	M3_W3_A2	0.82	110900	36000	0.49412
13	M2_W2_A1	0.78	86200	31000	0.33595	27	M3_W3_A3	0.82	110900	41000	0.62778
14	M2_W2_A2	0.78	86200	36000	0.42450						

Table 4: Dive conditions for the 27-point case

#	ID	M(-)	W(lbs)	A(ft)	C_{L}(-)
1	Dive1	0.87	61500	31000	0.19269
2	Dive2	0.87	110900	41000	0.55770

fuel requirements, thickness constraints, and a constraint for a straight leading edge (LE) and trailing edge (TE). A C_L for each cruise flight condition is specified corresponding to the Mach number, aircraft weight and altitude settings, as well as a moment constraint to limit trim drag. A summary of these constraints is given in Table 2.

2. *27-point Optimization*

Following Buckley and Zingg,[24] the 27-point optimization is completed using a trapezoidal quadrature rule with 3 quadrature points in the weight, altitude and Mach number axes. The specific flight conditions are given in Table 3. The lift coefficients for these conditions range from 0.217 to 0.771. Two operating conditions are also added with the constraint that $M_{max} < 1.4$ in order to keep shocks relatively weak under dive conditions. These operating conditions, which are shown in Table 4, are not included in the objective function but are constraints applied to the optimization.

Table 5: Average C_D and ML/D values in the prescribed flight envelope for the baseline shapes.

#	Design	$C_{D\text{ave}}$	$\Delta C_{D\text{ave}}\%$	ML/D_{ave}	$\Delta ML/D_{\text{ave}}\%$
1	Single-point	0.02422	0.00	13.735	0.00
2	27-point	0.02399	-0.98	13.831	0.69

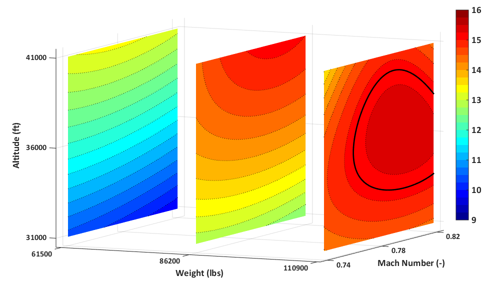

Figure 2: Aircraft ML/D contour plots for baseline designs. The 98% contour of the maximum ML/D is outlined in black.

3. Results

Overall performance comparisons are accomplished by computing average C_D and ML/D values throughout the flight envelope. As the flight envelope is quite large, computing a very accurate approximation of the average can be very computationally expensive. Flow evaluations at very fine intervals throughout the flight envelope would have to be computed. Instead, given computational resources, the approximation was made with a 3x3x3 grid of flight conditions which translates into a set of 27 flight conditions. As well, Simpson's rule is also used in three dimensions to provide a more accurate estimation of the average C_D and ML/D values. To ensure this integration method is valid, the centreline integral for each respective axis was computed on a finer scale. The evaluation of this fine scale integral compared to using Simpson's rule with a 3pt stencil shows at most a 0.1% difference in average C_D for all designs.

Table 5 shows the computed weighted averages for C_D and ML/D throughout the flight envelope for the baseline wing. This is compared with a wing that is optimized at the centre of the specified flight envelope. The value of each parameter is included along with its corresponding percent difference. The multipoint case shows an improvement in average performance over the range of specified flight conditions.

Figure 2 shows ML/D contours throughout the flight envelope for the multipoint optimized wing. These figures were created by taking the ML/D values at the 27 points and completing a tri-quadratic interpolation throughout the volume. Contour lines of 98% maximum ML/D are also included in these diagrams. This indicates the regions for an aircraft to operate within 2% of its minimum fuel consumption.

Since the 27-point optimization takes into account a large range of flight conditions, it is impossible to produce optimal performance at every flight condition. At many of the flight conditions, shocks are not present, but a few flight conditions, such as the low Mach number, high weight and high altitude condition as well as the high Mach number, high weight and high altitude condition, still have shocks present. For example, Figure 3 shows the entropy at a low Mach number, high weight, and high altitude condition where a shock is formed. The red region is the entropy due to the boundary layer and does not indicate a shock. Since there is still some wave drag present on the baseline design, there is potential for morphing to reduce the drag at these conditions. At conditions where no shocks are present on the baseline wing, morphing must reduce induced drag by improving the spanwise lift distribution.

IV. Morphing Optimizations

After the optimization and evaluation of the baseline shape, single-point morphing optimizations are then performed at each of the 27 operating conditions using the baseline geometry as the initial shape. These morphing optimizations only have freedom on a portion of the wing and are specifically constrained to be consistent with morphing actuation constraints. Twenty-seven optimizations are performed at multiple

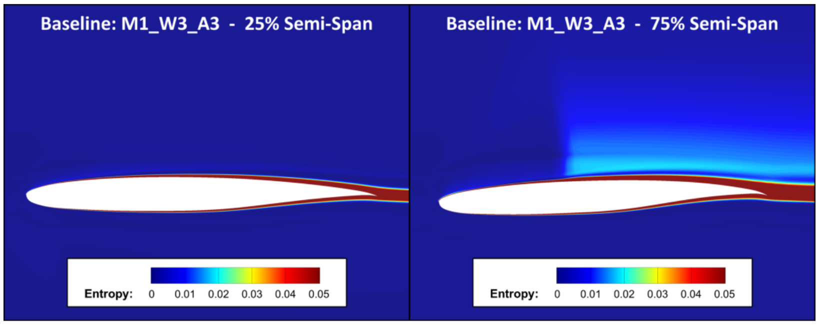

Figure 3: Entropy plots for the 27-point optimization with dive constraints at the low Mach number, high weight, high altitude condition.

Table 6: Design variables and constraints for each of the full morphing optimizations. Additional common design variables and constraints are given in Table 2.

Full Morphing				
	Lower bound	Variable/Constraint	Upper bound	#
Constraints	$+0.95\ t_{\text{orig}}$	Thickness	$+1.05\ t_{\text{orig}}$	325

Table 7: Average values through flight envelope for full morphing.

Type	C_{Dave}	$\Delta C_{\text{Dave}}\%$	ML/D_{ave}	$\Delta ML/D_{\text{ave}}\%$
Baseline	0.02399	0.00	13.831	0.00
Full Morph	0.02351	-1.99	14.109	2.01

flight conditions throughout the operating envelope so that an average integrated value of C_D and ML/D can be calculated. It is assumed that performance at intermediate operating conditions will be able to vary smoothly.

Five distinct types of morphing are studied. The first is full morphing, where the section shape of the entire wing is allowed to change, revealing the theoretical maximum benefit of such morphing. The second is trailing-edge morphing, which limits morphing to the trailing-edge portion of the wing, followed by upper-surface morphing, where only the upper surface of the wing is allowed to change, and leading-edge morphing, where only the leading edge of the wing is allowed to change shape. Finally, a sealed flap is considered where only flap-like rotations are allowed. The morphing results are compared with each other and with the multipoint optimized baseline wing. These comparisons provide insight into the most effective type of morphing.

A. Full Morphing Optimizations

This first type of morphing investigated is full morphing. Full morphing is defined as allowing all section variables as design variables, which are the z-coordinates of all control points, as well as the angle-of-attack. The control point at the leading-edge root is fixed to anchor the design. The wing leading-edge is constrained to be linear whereas the trailing-edge is free to move, which allows highly variable spanwise twist and section shapes to be achieved.

Constraints which are identical to the baseline optimization involve bound constraints on the design variables to limit unrealistic design variable values during early optimization iterations, a volume constraint to meet fuel requirements, and thickness constraints to account for structural requirements. For each optimization, a C_L is specified for each flight condition as well as a moment constraint to prevent excessive trim drag. All constraints summarizing the full morphing optimizations are summarized in Table 6.

These optimizations minimize the C_D value for their respective flight condition, which then was used to calculate the aircraft ML/D at that specific flight condition and the average ML/D and C_D values throughout the flight envelope, which are compared to the baseline in Table 7. There is a roughly 2%

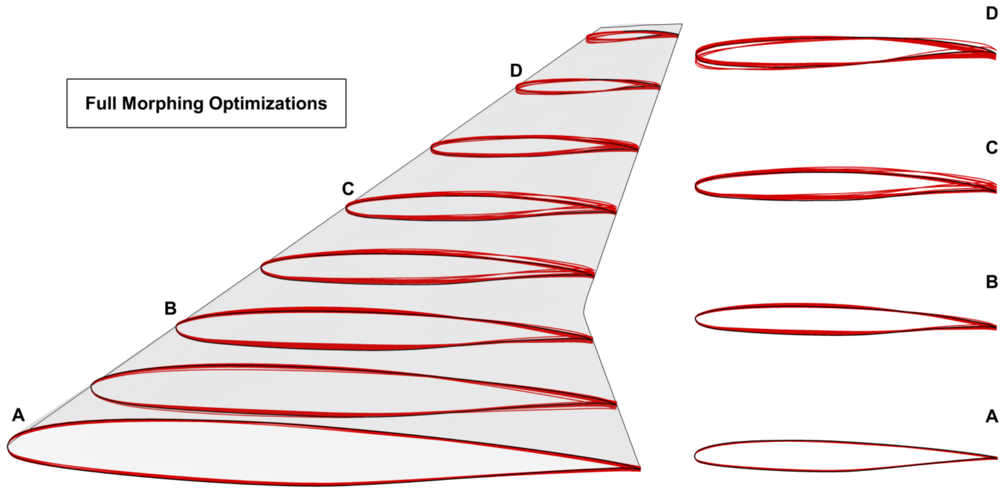

Figure 4: Shapes achieved by full morphing compared to the baseline. Black lines indicate the original wing, red lines indicate the morphing results.

improvement in average performance.

Figure 4 shows the variation of shapes seen by the entire range of full morphing optimizations. The black lines represent the original wing while each of the red lines represents a morphing optimization result. In general, the shape changes are not too extreme. This supports the idea that the initial wing geometry is a relatively good design for the flight conditions of interest. Some of the larger changes occur towards the tip of the wing where morphing tends to add some twist and thickness changes into the geometry relative to the baseline. These changes are believed to be theoretically achievable but the more robust current technologies typically focus on morphing only portions of the wing, such as FlexFoil mentioned earlier.

In order to examine how the performance changes in specific parts of the flight envelope, a series of contour plots were generated similar to the baseline ML/D contours. Figure 5a shows the contours of ML/D for full morphing. In this plot, the high weight, high Mach number and moderately high altitude condition shows the highest ML/D. When compared to the baseline contours, higher ML/D values can now be attained at higher Mach numbers, and the 98% contour has also been shifted towards higher Mach numbers and higher altitudes. This means that with morphing, better performance can be achieved at higher speeds and altitudes. This can be understood further by examining Figure 5b, which shows the change in ML/D due to full morphing. This is calculated by computing the difference between the full morphing ML/D contours and the baseline ML/D contours. Most of the change in ML/D occurs at the largest aircraft weight, with smaller performance benefits at the middle and lower weights. The condition with the largest maximum change in ML/D is located at the high Mach number, high weight, and high altitude condition, where there is roughly a 10% increase in ML/D. These conditions have lower C_L values and as a result the baseline shape already performs fairly well. Performance benefits from morphing at a specific weight also seem to have larger changes at higher Mach numbers, which were found to not be shock free in the previous section, signifying that morphing has some effect on reducing wave drag.

The changes in wave drag are confirmed by plotting entropy in the flow field across the wing. In the last chapter, it was shown that typically the low altitude and weight conditions had no shocks present on the baseline shapes but the high altitude and weight conditions did. The effect of morphing on these shocks can be seen in Figure 6. This image shows the baseline wing on the top and the full morphing result on the bottom at the low Mach number, high weight, and high altitude condition. It can be seen that a shock is initially present on the baseline, but full morphing removes this entirely.

Breaking the drag reductions down further, Figure 7 shows contours of the change in friction drag and pressure drag individually. Pressure drag reduction provides a majority of the drag reduction, as the magnitudes are much larger than the friction drag counterparts. This confirms that morphing primarily reduces wave and induced drag. This same trend is noticed in all other types of morphing in this work.

Figures 8 and 9 show aerodynamic comparisons of full morphing optimizations compared to the baseline

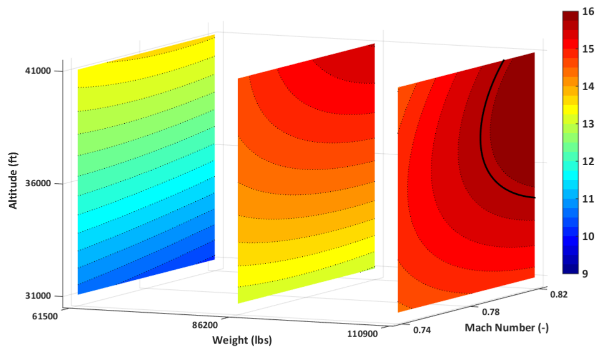

(a) ML/D contours through flight envelope. The 98% contour of the maximum ML/D is outlined in black.

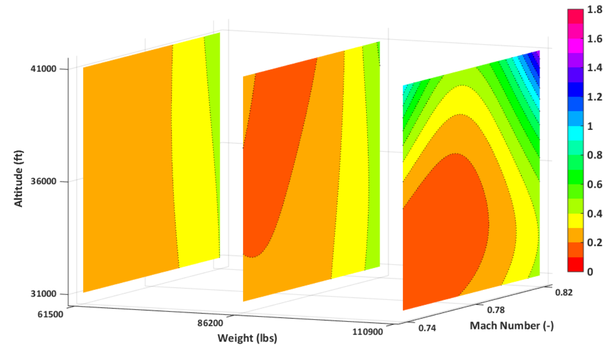

(b) $\Delta ML/D$ between baseline and morphing.

Figure 5: ML/D contour plots for full morphing.

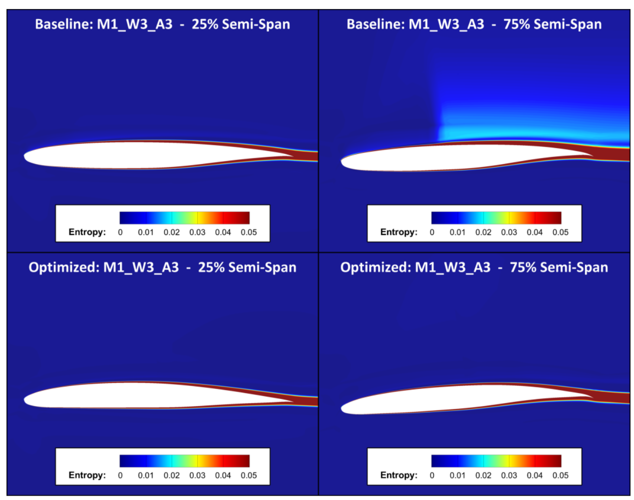

Figure 6: Entropy comparison before and after full morphing at the low Mach number, high weight, high altitude condition. The shock is fully removed.

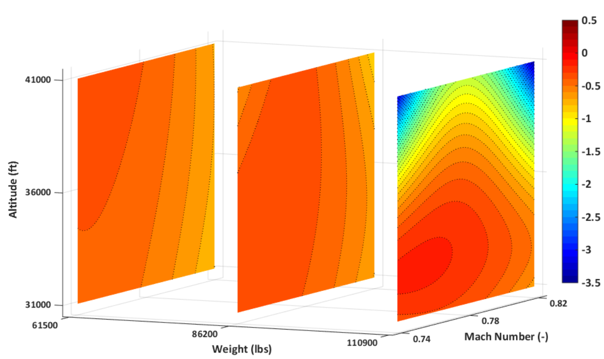

(a) $\Delta\ C_{Dp}$ in drag counts.

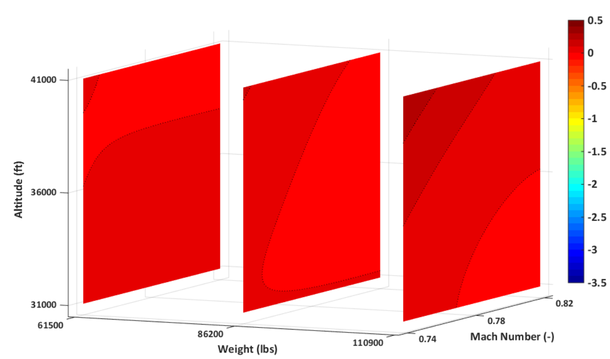

(b) $\Delta\ C_{Df}$ in drag counts.

Figure 7: $\Delta\ C_{Dp}$ and $\Delta\ C_{Df}$ in drag counts due to full morphing.

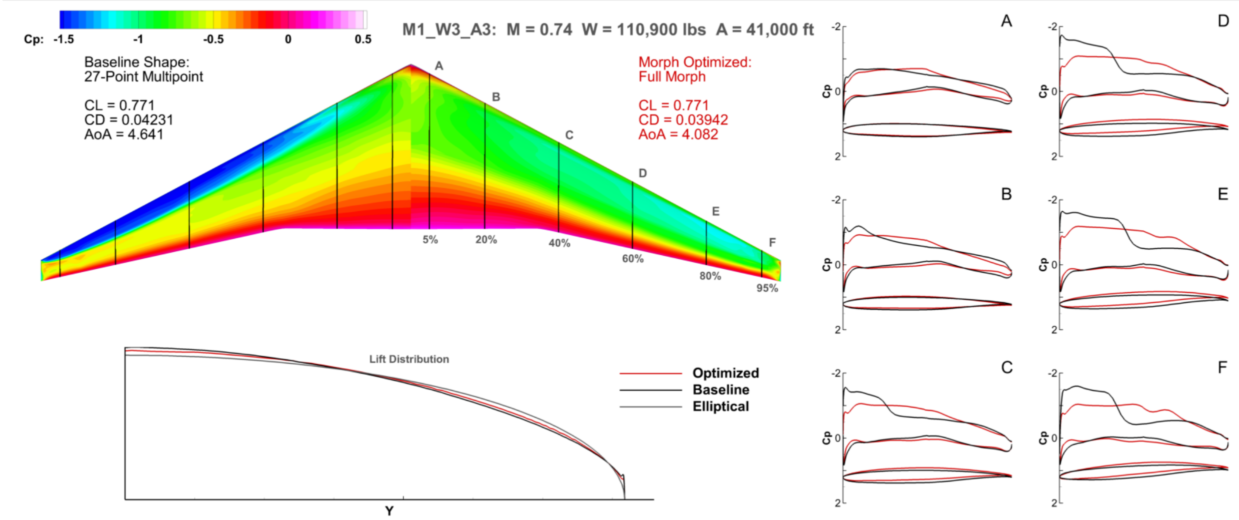

Figure 8: Comparison between the baseline wing and full morphing for the low Mach number, high weight, high altitude condition.

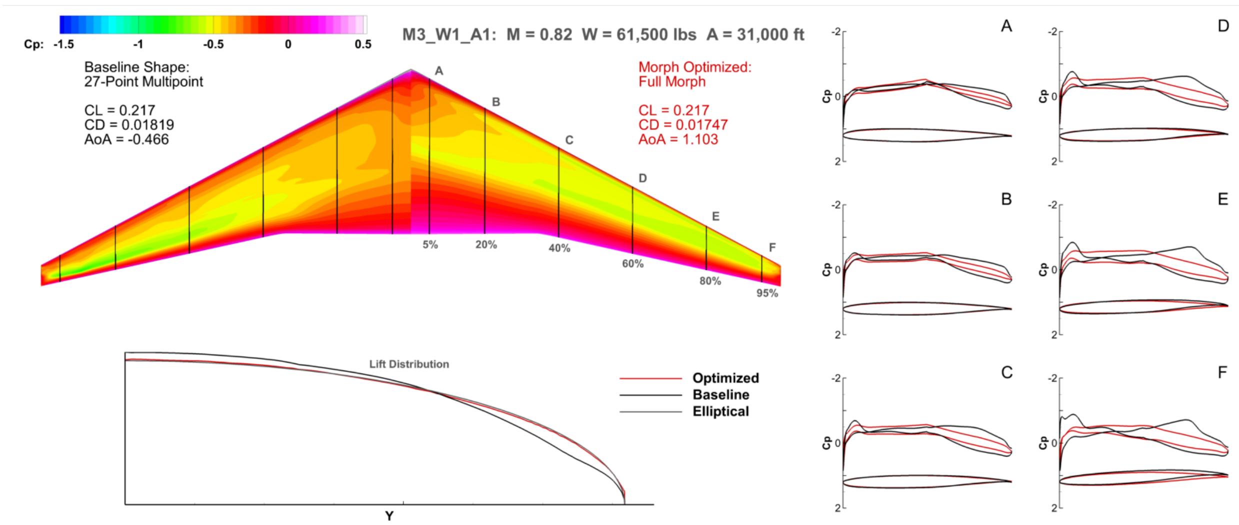

Figure 9: Comparison between the baseline wing and full morphing for the high Mach number, low weight, low altitude condition.

design at a high weight and low weight condition. The pressure contours and C_p plots show how the pressure changes with morphing, and the spanwise lift distributions and the entropy plots in Figure 6 give some indication of how induced and wave drag change because of morphing. Generally, from these figures, it can be noticed that if shocks are initially present, the optimizer tend to weaken them; otherwise, the spanwise lift distribution is improved instead. Figure 8 is an exception; since morphing is able to fully remove the shock, the lift distribution is able to improve concurrently. In summary, for operating conditions where the baseline wing has shocks, the primary effect of morphing is to reduce wave drag. For operating conditions where the baseline wing is shock free, the primary effect of morphing is to reduce induced drag by moving the spanwise load distribution towards an elliptical distribution.

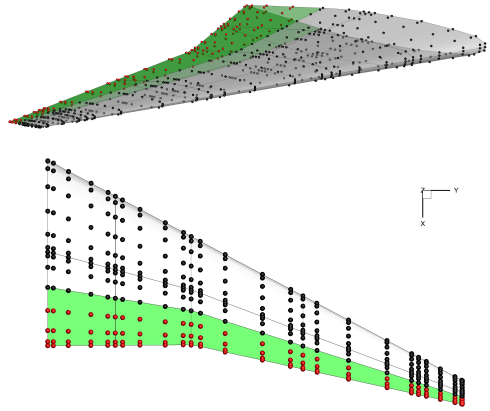

Figure 10: Trailing-edge morphing control point layout. Red points are design variables and black points are kept stationary. The region where morphing can occur is shown in green.

Table 8: Design variables and constraints for each of the trailing-edge morphing optimizations. Additional common design variables and constraints with the baseline optimization are given in Table 2.

Trailing-Edge Morphing				
	Lower bound	Variable/Constraint	Upper bound	#
Variables	x_{min} - 0.1*x_{max}	CPs x	x_{max} + 0.1*x_{max}	179
Constraints	+0.95 t_{orig}	Thickness	+1.05 t_{orig}	75
	+1.0 $\text{frac}_{\text{orig}}$	Chord Fraction	+1.0 $\text{frac}_{\text{orig}}$	153
	+1.0 SL_{orig}	Surface Length	+1.0 SL_{orig}	50

Table 9: Average values through flight envelope for trailing-edge morphing.

Type	C_{Dave}	$\Delta C_{\text{Dave}}\%$	ML/D_{ave}	$\Delta ML/D_{\text{ave}}\%$
Baseline	0.02399	0.00	13.831	0.00
TE Morph	0.02374	-1.04	13.978	1.06

B. Trailing-Edge Morphing Optimizations

Trailing-edge morphing is investigated in this section. Differing from full morphing, trailing-edge morphing has both the section and chordwise directions of the control points defined as design variables, which are the x and z-directions, as well as the angle-of-attack. Only the coordinates of control points on the rear 30% of the wing are set as design variables. The trailing-edge control point layout can be seen in Figure 10. Additional surface length constraints are also added at multiple spanwise locations to try to represent realistic materials that may be used to implement the actuation system. Since this is the trailing edge, two independent surface length constraints are applied at each location, one for the upper surface and one for the lower. This was done because if material was allowed to stretch, it would be hard to imagine this material stretching around the trailing edge. The other constraints are common to the full morphing optimizations as well. These include the design variable bounds, the volume constraint, the thickness constraints, the moment constraint, and a specified C_L. Trailing-edge morphing design variables are summarized in Table 8.

The resulting average ML/D and C_D values throughout the flight envelope are shown in Table 9. Trailing-edge morphing leads to a roughly 1% improvement in average performance, which is about half the benefit seen from full morphing.

Figure 11 shows the variation of shapes seen by the entire range of trailing-edge morphing optimizations. The black lines represents the original wing and each of the red lines represents a morphing optimization result. By comparing to Figure 4, the differences can be clearly seen. There is much less deviation from the original shape when freedom is only allowed near the trailing-edge. The trailing-edge morphing tends to

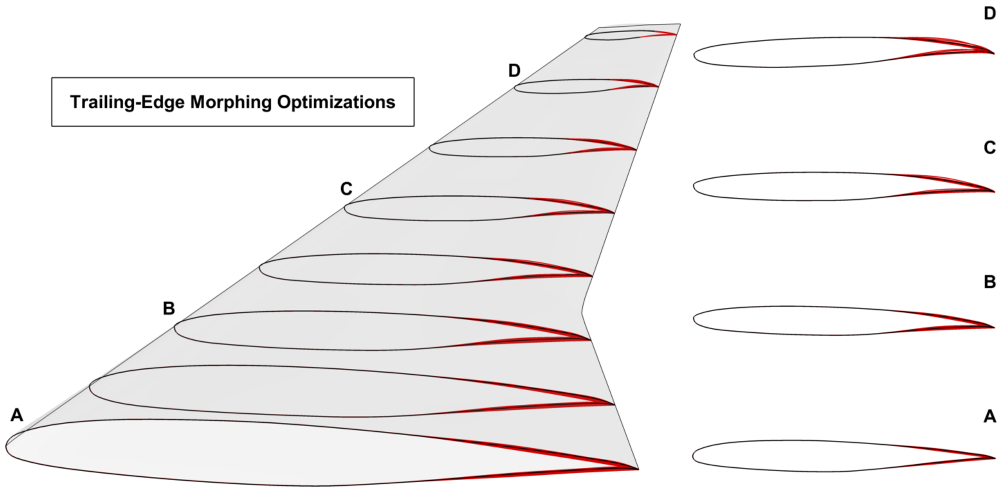

Figure 11: Shapes achieved by trailing-edge morphing compared to the baseline.

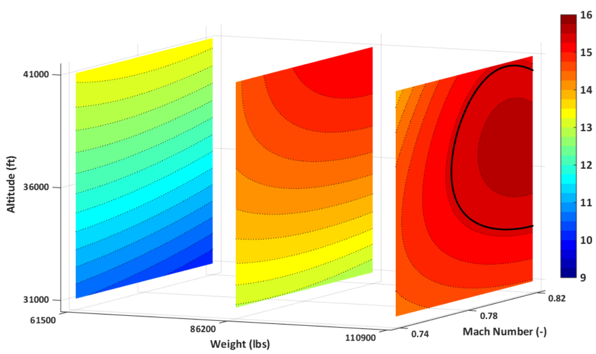

(a) ML/D contours through flight envelope. The 98% contour of the maximum ML/D is outlined in black.

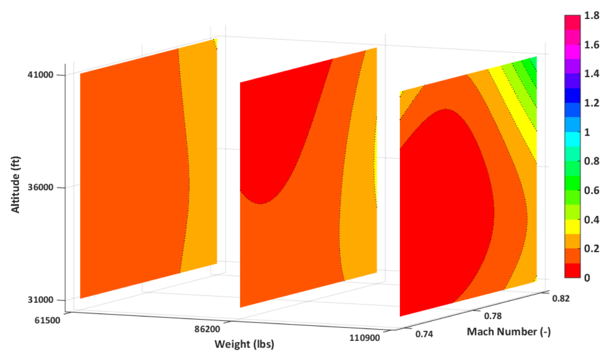

(b) $\Delta ML/D$ between baseline and morphing.

Figure 12: ML/D contour plots for trailing-edge morphing.

smooth out the upper surface and create more of a cambered lower surface. The effect of the surface length constraint can be seen, especially near the tip, as noticeably more camber is present on some shapes and no major flap-like deflections are present as were seen in prior studies.[4]

The ML/D contours in Figure 12 show characteristics similar to the full morphing plots. A shift in the maximum ML/D value towards higher Mach numbers is seen again but not to the same degree as the full morphing. The largest change in ML/D is located at the high Mach number, high weight, and high altitude condition, where there is roughly a 5.5% increase. Higher Mach numbers tend to show better performance improvements than lower Mach numbers, which suggests that trailing-edge morphing is primarily able improve to reduce wave drag and is not as effective at reducing induced drag. The reduction in wave drag is confirmed by plotting entropy on various cuts across the wing, as shown in Figure 13, which shows the effect of trailing-edge morphing at the low Mach number, high weight, and high altitude condition. The shock is not fully removed due to the limited amount of freedom, which differs from full morphing at this condition.

Figures 14 and 15 display aerodynamic comparisons for trailing-edge morphing. The low Mach number, high weight, and high altitude condition in Figure 14 has the strongest shock and highest maximum Mach number. For this condition, morphing is able to weaken this shock and lower the maximum Mach number but the lift distribution gets further from elliptical. For the conditions that do not have shocks, the spanwise lift distribution is able to improve. This is seen in Figure 15, where the lift distribution approaches the elliptical distribution for a planar wing, although the improvement in L/D is quite small.

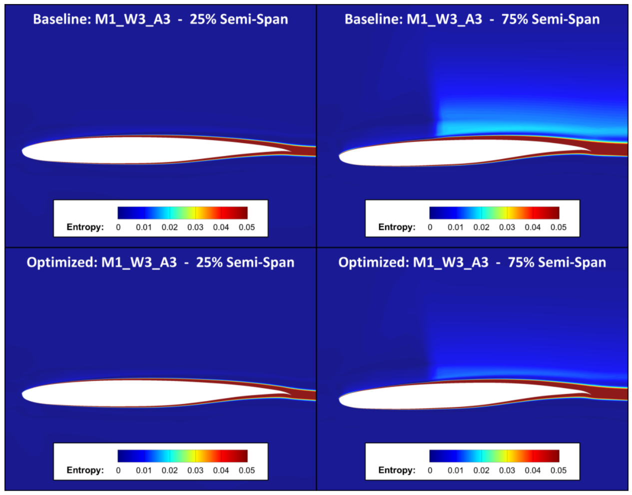

Figure 13: Entropy comparison before and after trailing-edge morphing at the low Mach number, high weight, high altitude condition.

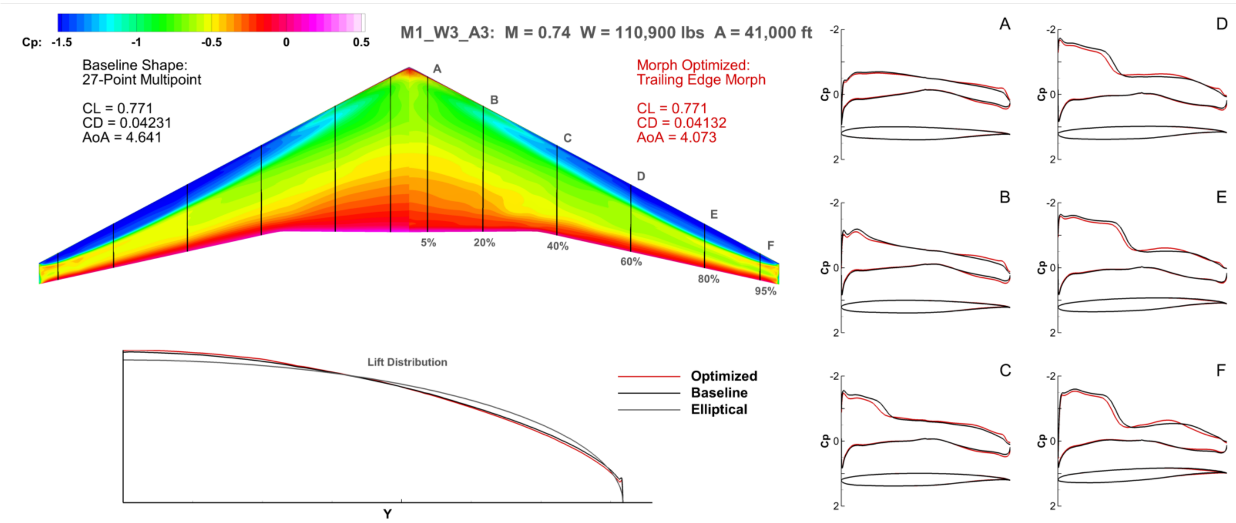

Figure 14: Comparison between the baseline wing and trailing-edge morphing for the low Mach number, high weight, high altitude condition.

C. Upper-Surface Morphing Optimizations

The third type of morphing considered is upper-surface morphing. It is set up by assigning design variables only on the top part of the wing. This allows for a morphing actuation system that is able to adapt the upper portion of the wing. The surface length constraint at each spanwise location is applied only as one constraint unlike the trailing-edge morphing, where there are two independent constraints applied. Other than changing which control points are initialized as design variables, the optimizations performed for upper-surface morphing are identical to the trailing-edge morphing optimizations. An overview of this optimization type is provided in Table 10.

Table 11 shows the computed averages for C_D and ML/D throughout the flight envelope resulting from the upper-surface morphing optimizations. There is roughly a 0.8% benefit seen on average through the use of upper-surface morphing.

Figure 16 demonstrates the shape changes seen by the upper-surface morphing optimizations. The black lines represent the original wing where each of the red lines represent a morphing optimization result. These shape changes are considerably less apparent than the changes due to full and trailing-edge morphing optimizations.

The ML/D contours in Figure 17, show that, in general, the maximum ML/D increases compared to

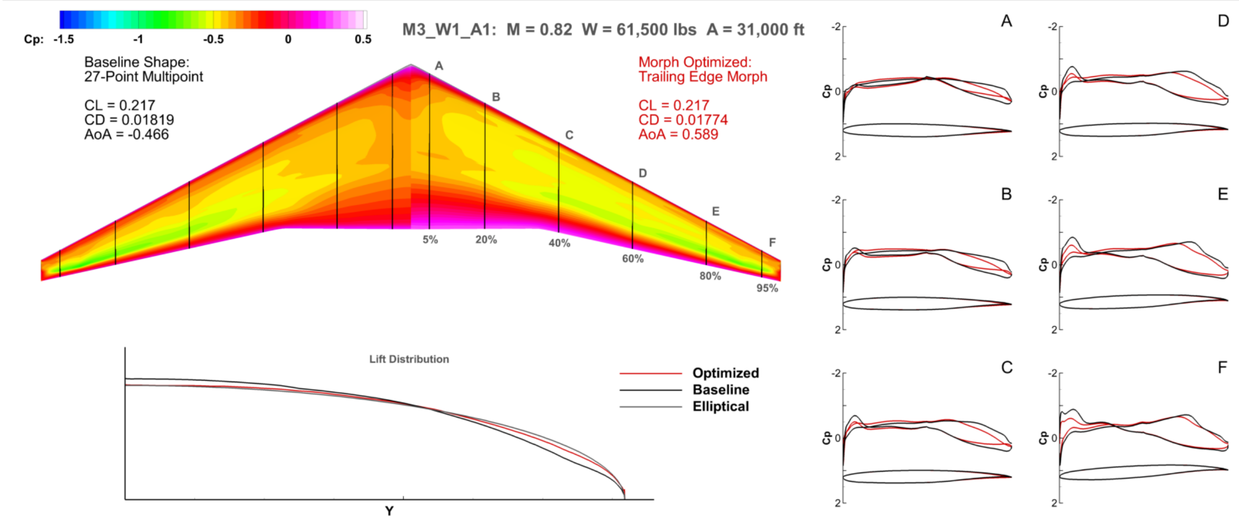

Figure 15: Comparison the between the baseline wing and trailing-edge morphing for the high Mach number, low weight, low altitude condition.

Table 10: Design variables and constraint descriptions for upper-surface morphing. Additional common design variables and constraints with the baseline optimization are given in Table 2.

Upper-Surface Morphing				
	Lower bound	Variable/Constraint	Upper bound	#
Variables	x_{min} - 0.1*x_{max}	CPs x	x_{max} + 0.1*x_{max}	340
Constraints	+0.95 t_{orig}	Thickness	+1.05 t_{orig}	325
	+1.0 $\text{frac}_{\text{orig}}$	Chord Fraction	+1.0 $\text{frac}_{\text{orig}}$	338
	+1.0 SL_{orig}	Surface Length	+1.0 SL_{orig}	25

Table 11: Average values through flight envelope for upper-surface morphing.

Type	C_{Dave}	$\Delta C_{\text{Dave}}\%$	ML/D_{ave}	$\Delta ML/D_{\text{ave}}\%$
Baseline	0.02399	0.00	13.831	0.00
US Morph	0.02378	-0.84	13.944	0.82

the baseline and moves to a higher Mach number and altitude for a specific weight. Again, the large changes in ML/D are mostly restricted to the high altitude, high weight and high Mach number conditions. Upper-surface morphing seems to have an effect on higher Mach number conditions regardless of weight, similar to trailing-edge morphing. As shocks typically form on the aft part of the upper surface of the wing and these types of morphing can alter their shapes near those locations, they both reduce the strength of the shock fairly well.

For the high altitude, high weight, and high Mach number condition, large improvements in ML/D are seen for upper-surface morphing, larger than for trailing-edge morphing. Figures 18 and 19 demonstrate the weakening of the shock strength over most of the span.

The low Mach number, high altitude, high weight condition, which corresponds to the largest C_L, shows small gains for the upper-surface morphing compared to the other morphing types. This may be caused by effective camber changes due to morphing the leading and trailing edges which the upper surface morphing cannot achieve. Very little change in ML/D again occurs as the weight decreases. Figure 20 shows that for the low weight conditions, upper-surface morphing is not able to improve the spanwise lift distribution.

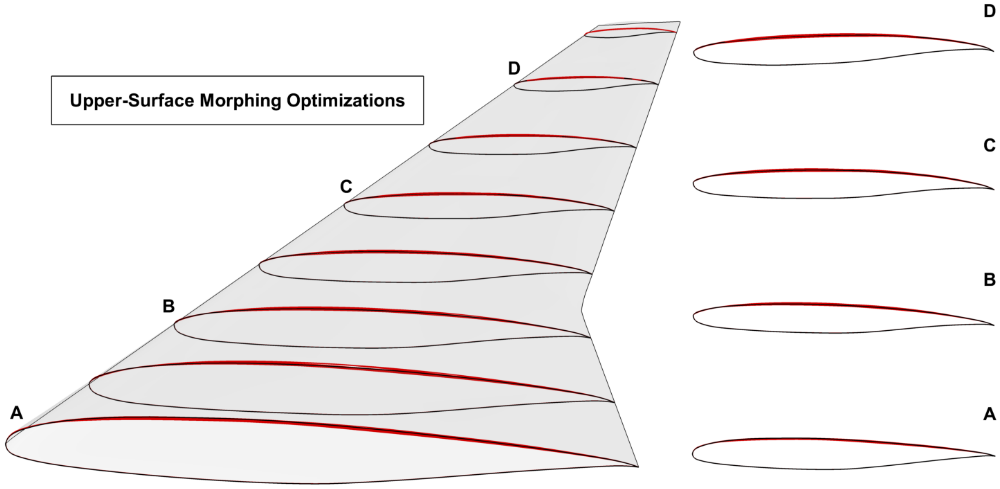

Figure 16: Shapes achieved by upper-surface morphing.

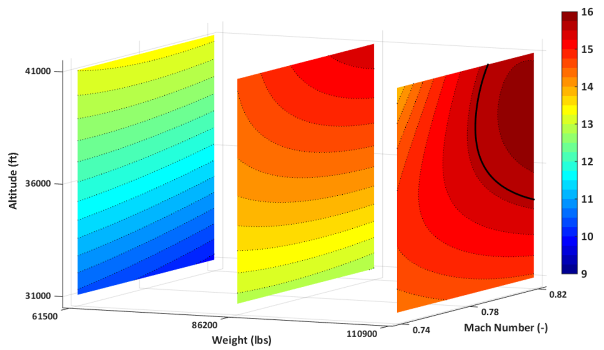

(a) ML/D contours through flight envelope. The 98% contour of the maximum ML/D is outlined in black.

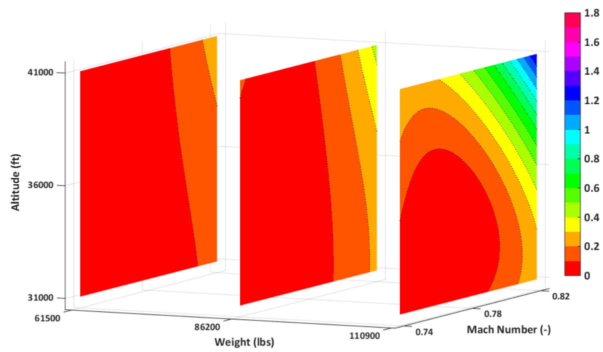

(b) ΔML/D between baseline and morphing.

Figure 17: Contour plots for upper-surface morphing.

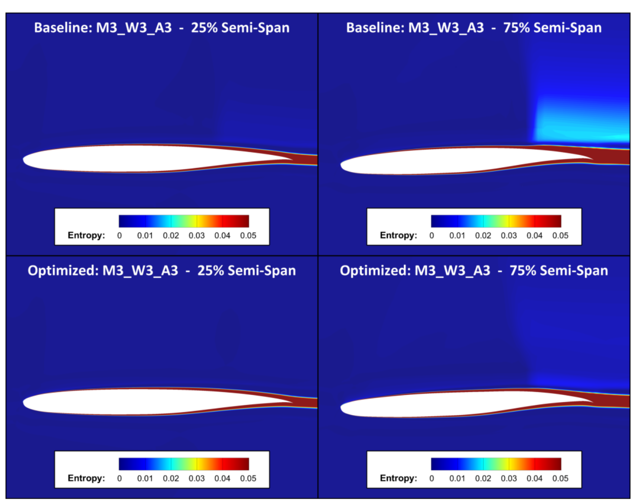

Figure 18: Entropy comparison before and after upper-surface morphing at the high Mach number, high weight, high altitude condition. There is a large reduction of the shock strength.

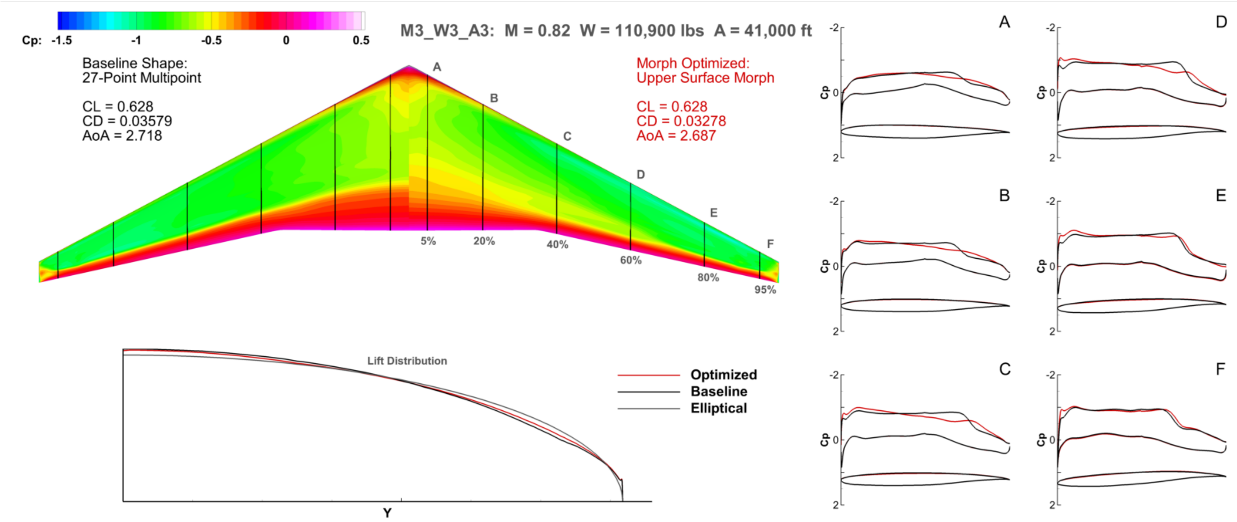

Figure 19: Comparison between baseline and upper-surface morphing for the high Mach number, high weight, high altitude condition.

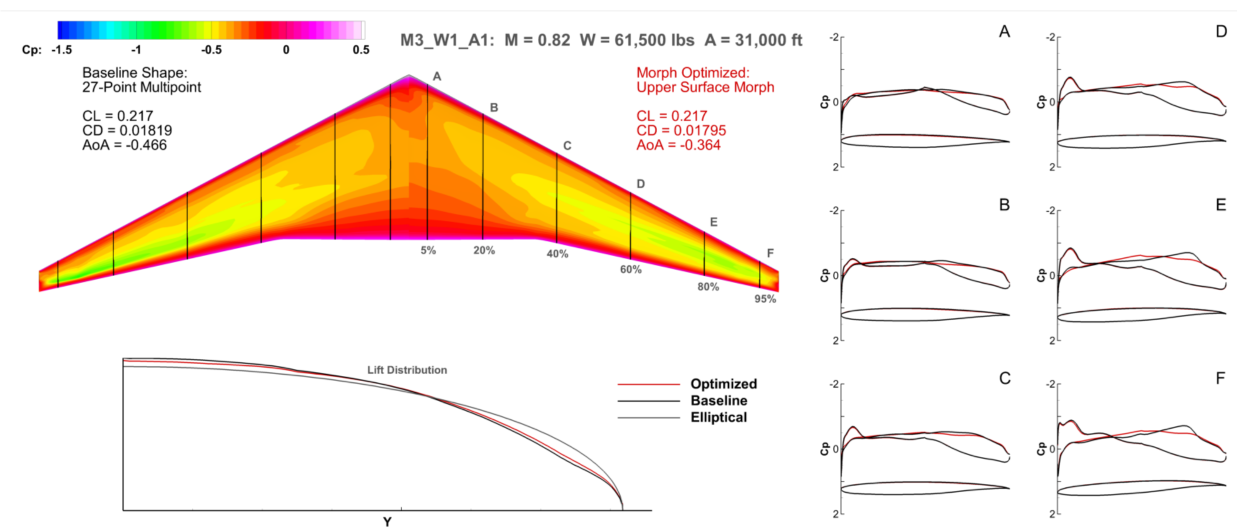

Figure 20: Comparison between baseline and upper-surface morphing for the high Mach number, low weight, low altitude condition.

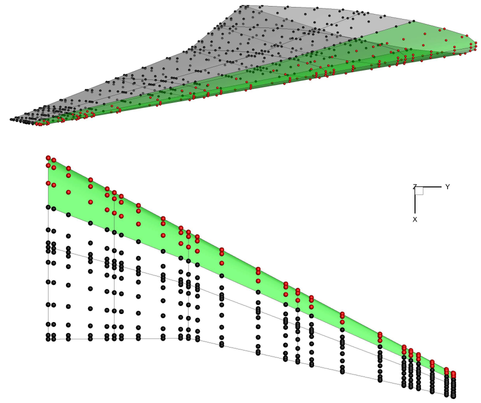

Figure 21: Leading-edge morphing control point layout. Red points are design variables and black points are kept stationary. The region where morphing can occur is shown in green.

Table 12: Design variables and constraints for each of the leading-edge morphing optimizations. Additional common design variables and constraints with the baseline optimization are given in Table 2.

	Leading-Edge Morphing			
	Lower bound	Variable/ Constraint	Upper bound	#
Variables	x_{min} - 0.1*x_{max}	CPs x	x_{max} + 0.1*x_{max}	179
Constraints	+0.95 t_{orig}	Thickness	+1.05 t_{orig}	75
	+1.0 $\text{frac}_{\text{orig}}$	Chord Fraction	+1.0 $\text{frac}_{\text{orig}}$	153
	+1.0 SL_{orig}	Surface Length	+1.0 SL_{orig}	25

Table 13: Average values through flight envelope for leading-edge morphing.

Type	C_{Dave}	$\Delta C_{\text{Dave}}\%$	ML/D_{ave}	$\Delta ML/D_{\text{ave}}\%$
Baseline	0.02399	0.00	13.831	0.00
LE Morph	0.02389	-0.40	13.879	0.35

D. Leading-Edge Morphing Optimizations

The fourth type of morphing investigated looks at the benefit due to leading-edge morphing. The leading-edge morphing is given the same constraints as the trailing-edge morphing, but the design variables are selected as the control points near to the leading edge, as shown in Figure 21. A breakdown of the design variables and constraints is provided in Table 12. This led to the averages for C_D and ML/D summarized in Table 13, which show that leading-edge morphing provides only about a 0.4% improvement in average performance.

The variation of shape changes caused by leading-edge morphing optimizations are shown in Figure 22. The original wing is depicted by the black lines while the morphing optimization results are depicted by the red lines. Again, the shape changes required are not too extreme and are comparable to the maximum shape change required by the trailing-edge morphing optimizations which were shown in Figure 11. There is again more shape change closer to the tip of the wing compared to the root.

The maximum ML/D in Figure 23 again increases compared to the baseline and moves to a higher Mach number and altitude for a specific weight. The large changes in ML/D are mostly restricted to the high altitude, high weight, and high Mach number conditions. This is noted in the entropy plots in Figure 24 since the change in shock strength is visible. At the same time, Figure 25 demonstrates that leading-edge morphing is able to improve the lift distribution at this condition. Overall, this confirms the larger ML/D improvements seen by leading-edge morphing compared to trailing-edge morphing in this region.

Smaller changes in ML/D again occur as the weight decreases. For the leading-edge morphing, virtually

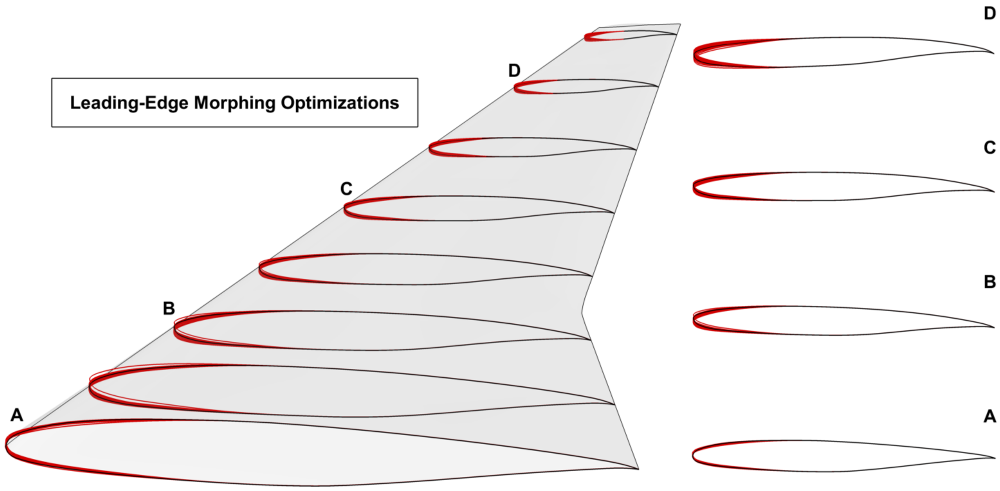

Figure 22: Shapes achieved by leading-edge morphing compared to the baseline.

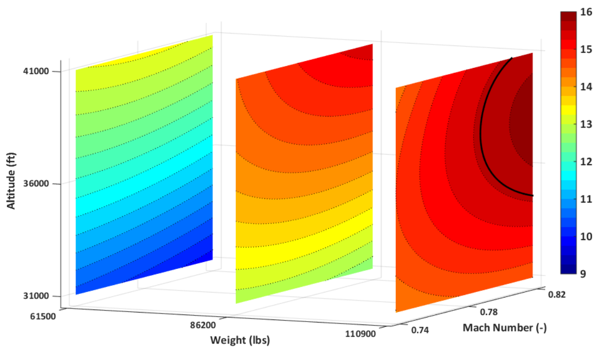

(a) ML/D contours through flight envelope. The 98% contour of the maximum ML/D is outlined in black.

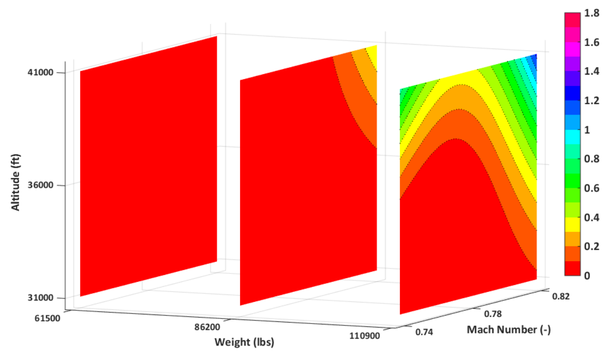

(b) ΔML/D between baseline and morphing.

Figure 23: Contour plots for leading-edge morphing.

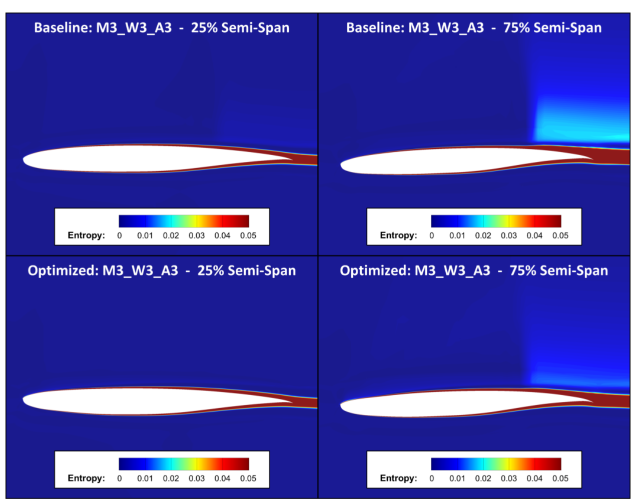

Figure 24: Entropy comparison before and after leading-edge morphing at the high Mach number, high weight, high altitude condition. Some reduction of the shock strength is present.

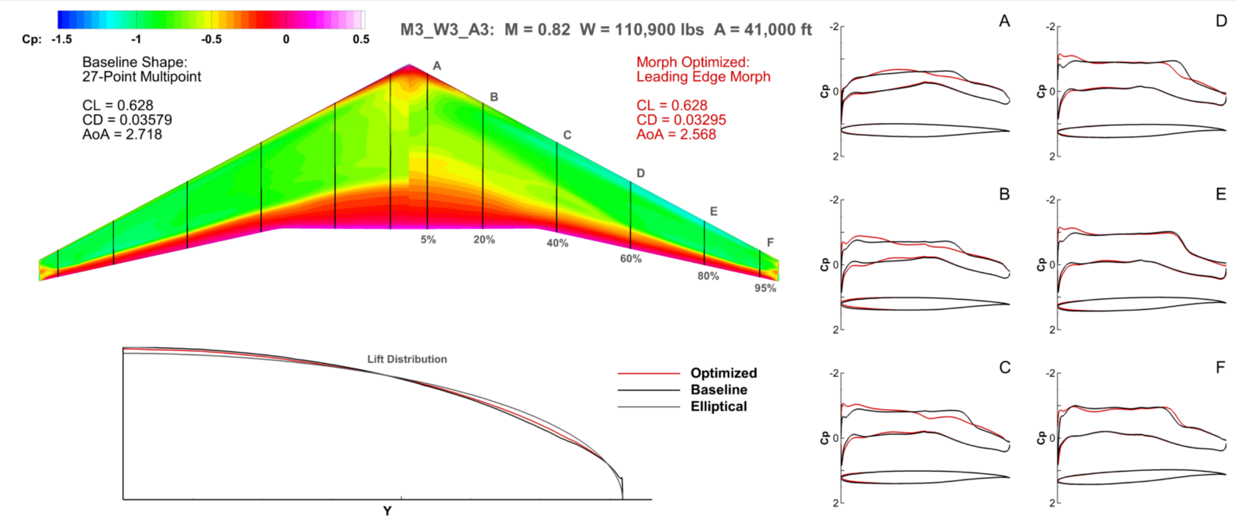

Figure 25: Comparison between the baseline wing and leading-edge morphing for the high Mach number, high weight, high altitude condition.

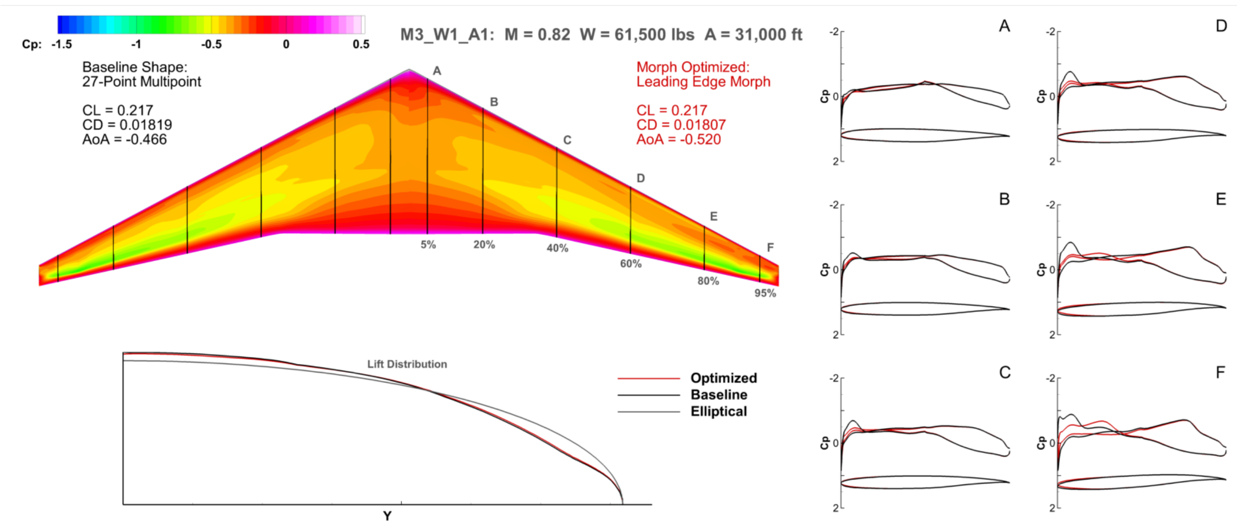

Figure 26: Comparison between the baseline wing and leading-edge morphing for the high Mach number, low weight, low altitude condition.

no benefit is realized at the lower aircraft weight values. Comparing Figures 26 and 20 to Figure 15, it is seen that for the low weight conditions, leading-edge morphing is not able to improve the spanwise lift distribution as well as both upper-surface and trailing-edge morphing.

Table 14: Design variables and constraints for each of the conventional flap optimizations. Additional common design variables and constraints with the baseline optimization are given in Table 2.

Flap Morphing				
	Lower bound	Variable/Constraint	Upper bound	#
Variables	-10.0°	Flap DVs	+10.0°	2

Table 15: Average values through flight envelope for the conventional flap.

Type	C_{Dave}	$\Delta C_{\mathrm{Dave}}\%$	ML/D_{ave}	$\Delta ML/D_{\mathrm{ave}}\%$
Baseline	0.02399	0.00	13.831	0.00
Flap	0.02387	-0.47	13.895	0.47

Table 16: Angle-of-attack and each flap angle at all flight conditions. All angles are in degrees. Positive flap angles denote downwards rotations.

Flight Condition	AoA	Flap 1	Flap 2	Flight Condition	AoA	Flap 1	Flap 2
M1_W1_A1	1.336	-1.914	-1.473	M2_W2_A3	2.248	0.223	0.458
M1_W1_A2	1.425	-1.129	-0.573	M2_W3_A1	1.734	-0.521	-0.126
M1_W1_A3	1.678	-0.286	0.395	M2_W3_A2	2.235	0.281	0.476
M1_W2_A1	1.469	-0.768	-0.160	M2_W3_A3	3.057	1.484	0.395
M1_W2_A2	1.714	0.195	0.882	M3_W1_A1	1.195	-2.303	-2.206
M1_W2_A3	2.195	1.335	1.908	M3_W1_A2	1.337	-1.862	-1.725
M1_W3_A1	1.723	0.252	0.940	M3_W1_A3	1.480	-1.243	-0.997
M1_W3_A2	2.254	1.324	1.805	M3_W2_A1	1.393	-1.644	-1.513
M1_W3_A3	3.607	2.716	0.802	M3_W2_A2	1.469	-0.871	-0.693
M2_W1_A1	1.335	-2.263	-1.971	M3_W2_A3	2.101	-0.430	-0.693
M2_W1_A2	1.439	-1.633	-1.278	M3_W3_A1	1.484	-0.837	-0.705
M2_W1_A3	1.671	-0.934	-0.504	M3_W3_A2	2.104	-0.407	-0.728
M2_W2_A1	1.491	-1.346	-0.968	M3_W3_A3	2.874	0.516	-0.854
M2_W2_A2	1.721	-0.567	-0.155				

E. Flap Optimizations

The last type of morphing studied involves a conventional sealed flap system. This is much simpler to obtain with a physical actuator. These optimizations use flap angles as design variables instead of B-spline control points. These angle variables can be described as rotations of the B-spline control points at specific spanwise locations. A hinge line is defined along the span of the wing at a constant chord-fraction location and the B-spline control points located aft of this line rotate about the hinge line to the specific flap angle. These optimizations define the hinge line at the aft 30% chord location and position the line in the centre of the airfoil to create a plain flap rotation. Since the wing geometry is swept and includes a crank, two independent flap sections are defined. There is one inboard and one outboard, and they are given two separate angles to optimize. As these design variables change during optimization, the control points are rotated about the hinge. Since the control points are rotated, there is more of a smooth transition between the wing and the flap compared to some flap systems which have a discontinuity before the flap surface. Although this is true, the modelled flap can be more closely related to the Adaptive Dropped Hinge Flap (ADHF) developed by Airbus.[9] Their flap employs a spoiler to cover the discontinuity and makes the entire wing a smooth surface. An overview of flap morphing design variables and constraints is provided in Table 14.

The resulting average C_D and ML/D are summarized in Table 15. The average performance improves throughout the flight envelope by about 0.5%. This is not as large of a benefit compared to some of the other types of morphing investigated earlier but may be worth pursuing given its simplicity.

Table 16 holds the angle-of-attack and the respective flap angles for all flight conditions. All flap angles are less than 3 degrees. In general, the inboard flap angle is larger than that of the outboard flap, which differs from the trailing-edge morphing optimizations.

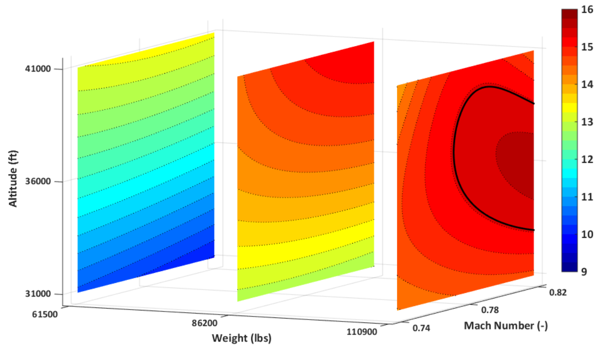

(a) ML/D contours through flight envelope. The 98% contour of the maximum ML/D is outlined in black.

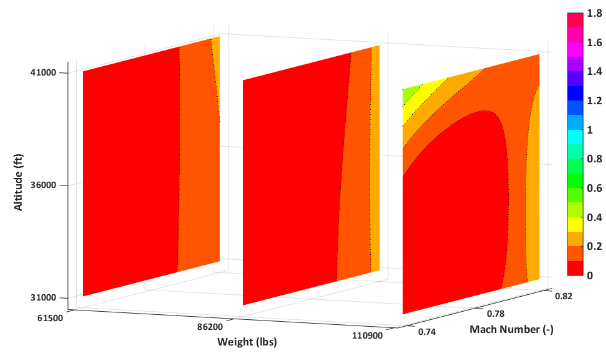

(b) $\Delta ML/D$ between baseline and morphing.

Figure 27: Contour plots for flap morphing.

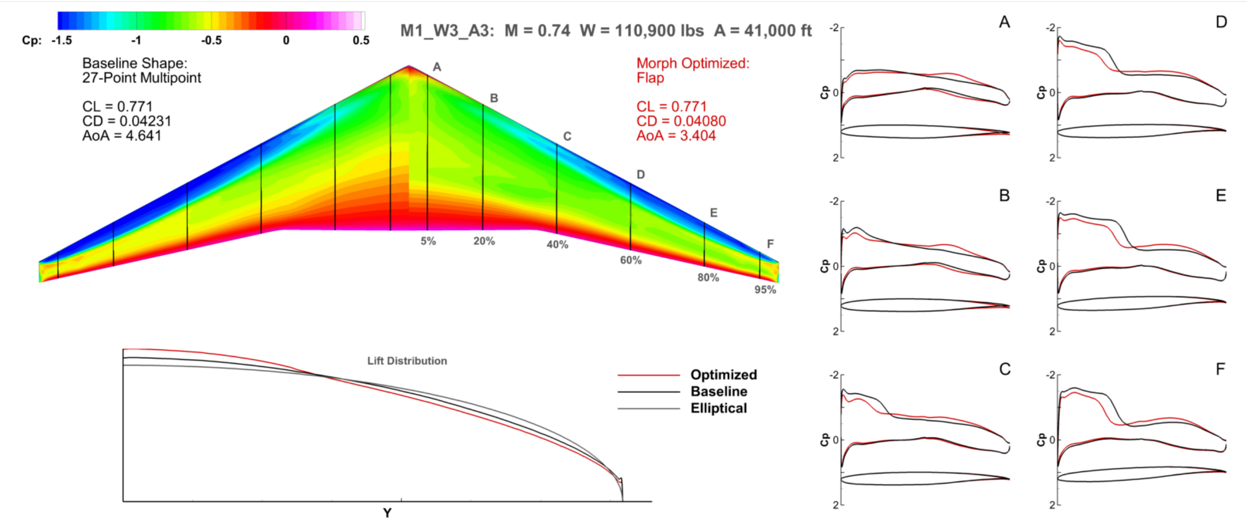

Figure 28: Comparison between the baseline wing and conventional flap for the low Mach number, high weight, high altitude condition.

The ML/D contours for the flap morphing in Figure 27a show that it is fairly similar to its trailing-edge morphing counterpart except for the high weight, high Mach number, and high altitude condition. This condition really is not affected much at all. Again, most of the benefits seen in the ML/D change plot in Figure 27b are at higher Mach numbers yet the maximum change is seen at the low Mach number, high weight, high altitude condition which corresponds to the largest C_L. Presumably, the differences between the trailing-edge morphing and conventional flap $\Delta ML/D$ contour plots must be caused by the additional freedom allowed in the trailing-edge morphing compared to the conventional flap. Trailing-edge morphing allows for some thickness changes which may assist with wave drag reductions at higher Mach numbers whereas flap morphing is restricted to two flap angles which effectively only change airfoil camber.

Aerodynamic comparisons of two flap optimizations are shown in Figures 28 and 29. The flight condition in Figure 28 displays a shock on the baseline wing and the optimizer uses the morphing freedom to weaken this shock. As the flaps are trying to reduce wave drag at these conditions, the spanwise lift distribution suffers when compared to trailing-edge morphing. This is due to the limited spanwise freedom of the conventional flap setup. In Figure 29, the baseline wing is shock free and the conventional flaps are able to improve the lift distribution just like trailing-edge morphing yet the conventional flap still does not improve the lift distribution to the same extent that trailing-edge morphing does, which provides further evidence that the smaller amount of spanwise freedom restricts the ability to reduce induced drag over a broad range of flight conditions.

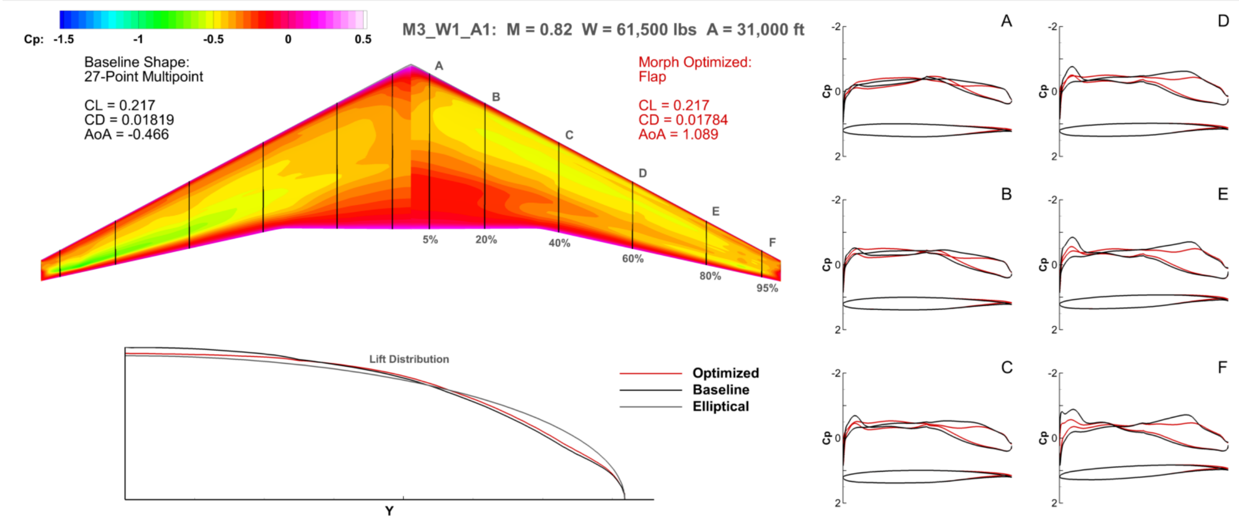

Figure 29: Comparison between the baseline wing and conventional flap for the high Mach number, low weight, low altitude condition.

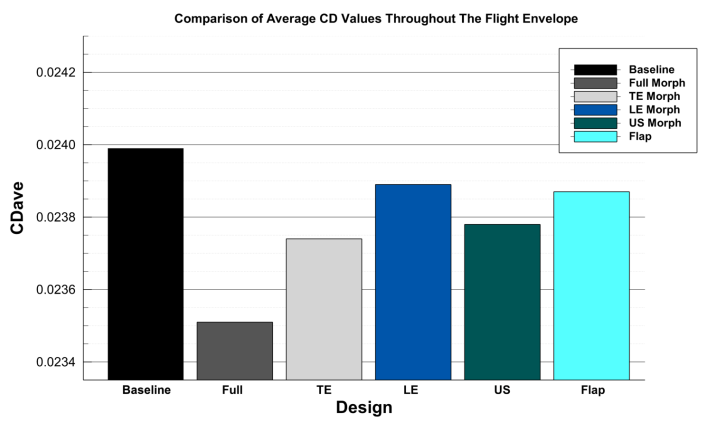

Figure 30: Comparison of C_{Dave} values for all morphing optimizations.

F. Overall Comparison

This section compares all the morphing optimizations together to examine the trade-offs present. Figures 30 and 31 summarize the average performance throughout the flight envelope for the baseline and all morphing optimizations. For both C_{Dave} and ML/D_{ave}, the full morphing optimizations clearly perform the best as expected. In terms of the more viable morphing concepts investigated, trailing-edge morphing proved to demonstrate the largest benefit. This option generates roughly half the benefit of full morphing. The difference between the two is quite large and if full morphing can be achieved, it would definitely be worth the effort. For the other morphing options, it is interesting to note that upper-surface morphing is the next best option followed by the sealed flap and then leading-edge morphing.

V. Conclusions

Aerodynamic shape optimization has been applied to a hypothetical regional class aircraft to explore the effects of morphing wings and evaluate the potential benefits this technology can have on an aircraft. Full morphing produces the largest benefit with about a 2% improvement in average aircraft performance over a range of cruise conditions. This can be compared to the roughly 1% change in aircraft performance from trailing-edge morphing. In general, if wave drag is present on the baseline wing, morphing reduces it. If the baseline wing is shock free at a particular flight condition, morphing reduces induced drag. Larger drag

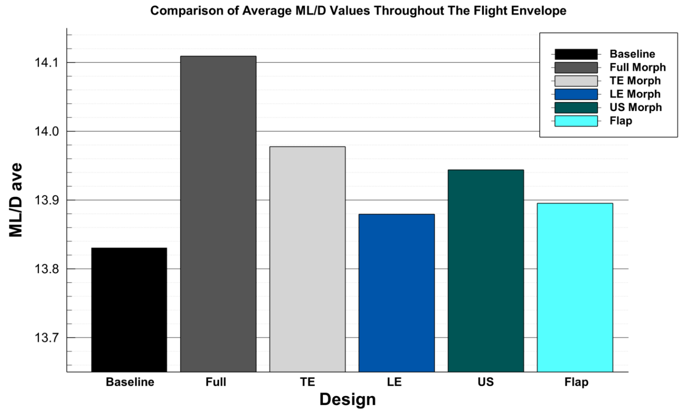

Figure 31: Comparison of ML/D_{ave} values for all morphing optimizations.

reductions are seen at high Mach number and high C_L conditions. Different effects on performance were demonstrated by constraining morphing to various portions of the wing surface. Trailing-edge morphing improves performance at all conditions as it can reduce either wave or induced drag.

The effect of using a simpler morphing system was also demonstrated through evaluating a sealed flap. Even though the morphing was performed on the same part of the wing, the limited amount of freedom allowed with the flap restricted the performance benefits compared to the trailing-edge morphing. It was noticed that at conditions where trailing-edge morphing was able to minimize wave drag easily the flap did not do this as well. Nevertheless, this option could be worth pursuing due to its simplicity.

Overall, with the exception of the simple flap, the benefits of morphing may not be sufficiently large to justify the increased complexity, weight, and power requirements. Given that the largest benefits of morphing arise from eliminating or weakening shock waves, it may be better to utilize morphing to enable speed increases rather than drag reductions at current speeds. Similarly, morphing may show larger benefits on faster aircraft such as business jets and twin-aisle aircraft.

References

[1] Airbus, *Sustainable Aviation: Aviation Environmental Roadmap*, France, April 2013.

[2] Barbarino, S., Bilgen, O., Ajaj, R., Friswell, M., and Inman, D., "A Review of Morphing Aircraft," *Journal of Intelligent Material Systems and Structures*, Vol. 22, 2011, pp. 823–877.

[3] Kota, S., Osborn, R., G. Ervin, G., and Maric, D., "Mission Adaptive Compliant Wing-Design, Fabrication and Flight Test," *Proceedings of the RTO Applied Vehicle Technology Panel(AVT) Symposium, The NATO Science and Technology Organization*, Brussels, 2009.

[4] Martins, J. and Lyu, Z., "Aerodynamic Shape Optimization of an Adaptive Morphing Trailing-Edge Wing," *Journal of Aircraft*, Vol. 52, November 2015, pp. 1951–1970.

[5] Rodriguez, D., Aftosmis, M., Nemec, M., and Anderson, G., "Optimized Off-Design Performance of Flexible Wings with Continuous Trailing-Edge Flaps," *AIAA Paper 2015-1409*, 2015.

[6] Kintscher, M., Wiedemann, M., Monner, H., Heintze, O., and Kuhn, T., "Design of a smart leading edge device for low speed wind tunnel tests in the European project SADE," *International Journal of Structural Integrity*, Vol. 2, No. 4, 2011, pp. 383–405.

[7] Stanewsky, E., "Adaptive Wing and Flow Control Technology," *Progress in Aerospace Sciences*, Vol. 37, 2001, pp. 583–667.

[8] Zingg, D. W., Diosady, L., and Billing, L., "Adaptive Airfoils for Drag Reduction at Transonic Speeds," *AIAA Paper 2006-3656*, 2006.

[9] Sutcliffe, M., Reckzeh, D., and Fischer, M., "HICON Aerodynamics – High Lift Aerodynamics Design for the Future," *International Congress of the Aeronautical Sciences*, 2006.

[10] Hicken, J. E. and Zingg, D. W., "A Parallel Newton-Krylov Solver for the Euler Equations Discretized Using Simultaneous Approximation Terms," *AIAA Journal*, Vol. 46, No. 11, 2008, pp. 2773–2786.

[11] Hicken, J. E. and Zingg, D. W., "Aerodynamic Optimization Algorithm with Integrated Geometry Parameterization and Mesh Movement," *AIAA Journal*, Vol. 48, No. 2, 2010, pp. 401–413.

[12] Osusky, M. and Zingg, D. W., "A Parallel Newton-Krylov-Schur Flow Solver for the Navier-Stokes Equations Discretized Using Summation-By-Parts Operators," *AIAA Journal*, Vol. 51, No. 12, 2013, pp. 2833–2851.

[13] Osusky, L., Buckley, H., Reist, T., and Zingg, D. W., "Drag Minimization Based on the Navier-Stokes Equations Using a Newton-Krylov Approach," Vol. 51, No. 12, 2015, pp. 2833–2851.

[14]Gagnon, H. and Zingg, D. W., "Two-Level Free-Form and Axial Deformation for Exploratory Aerodynamic Shape Optimization," Vol. 53, No. 7, 2015, pp. 2015–2026.

[15]Lee, C., Koo, D., Telidetzki, K., Buckley, H., Gagnon, H., and Zingg, D. W., "Aerodynamic Shape Optimization of Benchmark Problems Using Jetstream," *53rd AIAA Aerospace Sciences Meeting*, No. AIAA-2015-0262, Kissimmee, FL, January 2015.

[16]Koo, D. and Zingg, D. W., "Investigation into Aerodynamic Shape Optimization of Planar and Nonplanar Wings," *AIAA Journal. doi:10.2514/1.J055978*, 2017.

[17]Reist, T. and Zingg, D. W., "High-Fidelity Aerodynamic Shape Optimization of a Lifting-Fuselage Concept for Regional Aircraft," *Journal of Aircraft*, Vol. 54, No. 3, 2017, pp. 1082–1097.

[18]Truong, A., Oldfield, C., and Zingg, D. W., "Mesh Movement for a Discrete Adjoint Newton-Krylov Algorithm for Aerodynamic Optimization," Vol. 46, No. 7, 2008, pp. 16951704.

[19]Osusky, M. and Zingg, D. W., "Parallel Newton-Krylov-Schur Solver for the Navier-Stokes Equations Discretized Using Summation-By-Parts Operators," *AIAA Journal*, Vol. 51, No. 12, 2013, pp. 2833–2851.

[20]Gill, P., Murray, W., and Saunders, M. A., "SNOPT: An SQP Algorithm for Large-Scale Constrained Optimization," *SIAM Review*.

[21]Embraer Commercial Aircraft, *Embraer 190 Airport Planning Manual*, 2005.

[22]U.S. Government Printing Office, *U.S. Standard Atmosphere 1976*, 1976.

[23]Raymer, D. P., *Aircraft Design: A Conceptual Approach*, American Institute of Aeronautics and Astronautics, 5th ed., 2012.

[24]Buckley, H. and Zingg, D. W., "Approach to Aerodynamic Design Through Numerical Optimization," *AIAA Journal*, Vol. 51, No. 8, 2013.